https://doi.org/10.5194/egusphere-2026-6135
Preprint. Discussion started: 22 November 2026
© Author(s) 2026. CC BY 4.0 License.

A minimal model for soil-erosion connectivity in drylands

Selim Haj Ali[1,2], Shubham Tiwari[3,4], Marc-Thorsten Hütt[1], John Wainwright[3], and Laura Turnbull[3]

[1]School of Science, Constructor University, Bremen, Germany
[2]Global Systems Institute, University of Exeter, Exeter, UK
[3]Department of Geography, Durham University, Durham, UK
[4]Jornada Experimental Range, New Mexico State University, New Mexico, USA

Correspondence: Selim Haj Ali (s.haj-ali@exeter.ac.uk)

Abstract. Soil erosion is a major contributor to the degradation of soil resources underpinning ecosystem functioning across terrestrial systems worldwide. Yet existing erosion models often require extensive parameterisation and computational resources, limiting their spatiotemporal generalisability. Here, we adapt a dissipative sandpile model, incorporating spatially heterogeneous vegetation and microtopography, to reproduce erosion patterns and provide mechanistic insights into connectivity-driven dynamics in drylands. We benchmark our model against a process-based erosion model and field observations, using spatial connectivity patterns and event-scale sediment exports. We introduce a structural connectivity (SC) measure to predict erosion hotspots and find strong correlations ($\rho \approx 0.88$) with the landscape's functional connectivity (FC), particularly in shrubland. Using generated landscapes, we disentangle the contributions of vegetation-microtopography coupling, vegetation cover, and patchiness. We find that this coupling, associated with shrub encroachment, can counteract and reverse the effect of vegetation loss alone on connectivity and the propensity for large erosion events. Besides, SC-FC correlations are inversely related to the avalanche scaling exponent (mean Pearson correlation ≈ 0.6), indicating improved predictability of erosion hotspots in landscapes prone to large-scale geomorphic feedback. Our results demonstrate how a minimal sandpile framework can isolate mechanisms underlying connectivity-driven erosion while providing a computationally efficient complement to detailed process-based models.

1 Introduction

33% of the Earth's soils are already degraded, a figure that is expected to reach 90% by 2050 Food and Agriculture Organization of the United Nations (2020); Food and Agriculture Organization of the United Nations and Intergovernmental Technical Panel on Soils (2015). Soil erosion is a major contributor to soil degradation Ravi et al. (2010), threatening ecosystem functioning and productivity across affected regions. These issues are particularly acute across the world's drylands which are characterised by sparse, patchy vegetation cover. Understanding how soil erosion will change in the future under an intensifying climate, under increased human-induced pressures, or under restoration efforts, requires the development of robust soil-erosion modelling approaches.

Many conceptual and theoretical (e.g. Strahler (1980); Kirkby (1996)), empirical (e.g. Wischmeier and Smith (1978); Renard (1997)), and process-based models (e.g. Schindewolf and Schmidt (2012); Ciampalini et al. (2012); Bout and Jetten (2018);

https://doi.org/10.5194/egusphere-2026-6135
Preprint. Discussion started: 22 November 2026
© Author(s) 2026. CC BY 4.0 License.

Wainwright et al. (2008a)) have emerged to develop and refine our understanding of the processes involved in soil erosion. Many erosion models remain insufficiently validated against observational data Borrelli et al. (2021). As with all modelling, soil-erosion modelling involves a trade-off between model complexity and interpretability Bennett et al. (2013); Jakeman and Hornberger (1993): Highly parameterised models are generally able to better replicate field-based observations, thereby increasing confidence in their predictive capacity. However, this confidence can come at the cost of reduced generalisability to larger spatial scales and to extreme events. Whilst extreme events, by definition, are rare, they are often of particular interest, and extrapolation to them can propagate error and uncertainty model simulations Devitt et al. (2021); Diodato (2006).

A variety of models describe erosion-accumulation processes under natural vegetation, each with different approaches to simulating runoff, erosion, and sediment transport Baartman et al. (2020). These include process-based models like EROSION3D Schindewolf and Schmidt (2012); Schmidt (1991), LandSoil Ciampalini et al. (2012); Govers et al. (1994), and OpenLISEM Bout and Jetten (2018), which incorporate detailed process descriptions and have been tested in agricultural and semi-natural landscapes. Others, such as FullSWOF_2D Matteo et al. (2018); Delestre et al. (2017), focus on shallow-water equations for overland flow, while models like Watersed Landemaine (2016) are data-driven. These models vary significantly in their representation of key processes such as infiltration, runoff generation, and flow routing, as well as in their data requirements and complexity.

Ultimately, quantitative models exist on a spectrum: At one extreme, accuracy is paramount and models are evaluated according to their realism, their ability to reproduce and predict the phenomenon of interest, and their mechanistic representation of the processes that generate it. At the other extreme, approaches rooted in complex systems theory deliberately omit finer-scale detail to isolate the minimal interactions that are responsible for emergent system-level patterns. From this perspective, adding finer detail can obscure the complex phenomena in question, resulting in unsolvable models that inevitably require later approximations Batterman (2002). Therefore, approaches rooted in complex systems theory often take highly idealised forms caricaturing the essential physics of a given phenomenon Goldenfeld (2018).

Improving our understanding of soil erosion as a driver of land degradation requires approaches that can be applied where the data needed to parametrise and validate detailed process-based models are limited. This need is particularly important in drylands, where field observations are often sparse and the spatial heterogeneity of vegetation and microtopography can result in complex patterns of runoff and erosion. The contrast between different model types therefore raises the central question of whether a minimal model based only on threshold dynamics and redistribution can reproduce spatial and event-scale patterns of erosion while also providing insight into the mechanisms from which these patterns emerge. Here, our aim is to explore the capacity of a minimal sandpile model Bak et al. (1988); Manna (1991); Olami et al. (1992) to reproduce and help explain these patterns. The value of such an approach is that in comparison to geomorphological models grounded in physical processes, sandpile models are minimal, physics-free representations of threshold dynamics and redistribution, where particles serve as abstract units of load or potential that topple once local thresholds are exceeded. Therefore, using a sandpile model, we can test whether soil erosion patterns can emerge from a small number of interactions, with fewer data and parameter requirements than detailed process-based models.

https://doi.org/10.5194/egusphere-2026-6135
Preprint. Discussion started: 22 November 2026
© Author(s) 2026. CC BY 4.0 License.

Specifically, we: (1) evaluate the capacity of a dissipative sandpile model to reproduce key erosion patterns observed in a more complex process-based model and field data; (2) explore the influence of vegetation clustering and microtopography on hillslope erosion dynamics in both empirical (natural) and generated (synthetic) landscapes, with the latter constructed using data-driven algorithms; and (3) explore the utility of connectivity measures and avalanche distributions for analysing the system's collective dynamics of erosion processes in dryland environments.

2 Methods

This section outlines the sandpile framework, the field data and process-based model used for evaluation, the data-driven landscape generation algorithm, and the analytical tools used to characterise erosion dynamics.

2.1 The sandpile model

Water-driven soil erosion is modelled using a directed, dissipative stochastic sandpile model. Within the model, particles represent abstract units of sediment-mobilisation potential that accumulate locally and are redistributed over a topographically defined lattice when a local threshold is exceeded. In the context of a real-world erosion event, this potential can be interpreted as the local capacity for runoff to detach and transport sediment. The correspondence between hillslope erosion processes and their representation within the sandpile model is summarised in Table 1.

Within the model framework, we explore two flow-routing approaches: (i) *probabilistic descent dynamics* based on elevation differences between neighbouring nodes, and (ii) *deterministic steepest descent dynamics*. The latter mimics the flow-routing approach used in MAHLERAN and many of the other erosion models mentioned previously. This allows for a direct comparison between the two models, see Section 2.3.

2.1.1 Sandpile model topology, dynamics and rationale

Hillslopes are represented as 2-D directed anisotropic acyclic lattices (formally directed acyclic graphs, DAG Aho et al. (2023); Cossart and Fressard (2017)) where nodes can have up to three downslope neighbours and where the lowest layer acts as the outflow and has no out-degree (Figure 1a). Each lattice obeys lateral periodic boundary conditions where particles leaving the right-hand side of the system end up in the corresponding left-hand side, and vice versa.

Dissipation Olami et al. (1992) of particles occurs at two levels: deterministically from the outflow layer, and probabilistically across the lattice proportionally to the local vegetation density. Graph directedness Dhar and Ramaswamy (1989) represents whether particles are allowed to propagate between neighbouring nodes, i.e., from high-elevation (source) to lower-elevation (target) nodes. Stochasticity Manna (1991) refers to both the random addition of particles to the lattice and the subsequent random redistribution of particles after toppling, proportional to the elevation difference between the source and the target nodes.

The components of the model are formalised as follows. Let L be a $(n_y \times n_x)$ 2-D lattice of N nodes and E links, with n_y vertical layers and n_x horizontal layers. Each node $i \in L$ has a number of particles s_i (dynamic), and is characterised by a

https://doi.org/10.5194/egusphere-2026-6135
Preprint. Discussion started: 22 November 2026
© Author(s) 2026. CC BY 4.0 License.

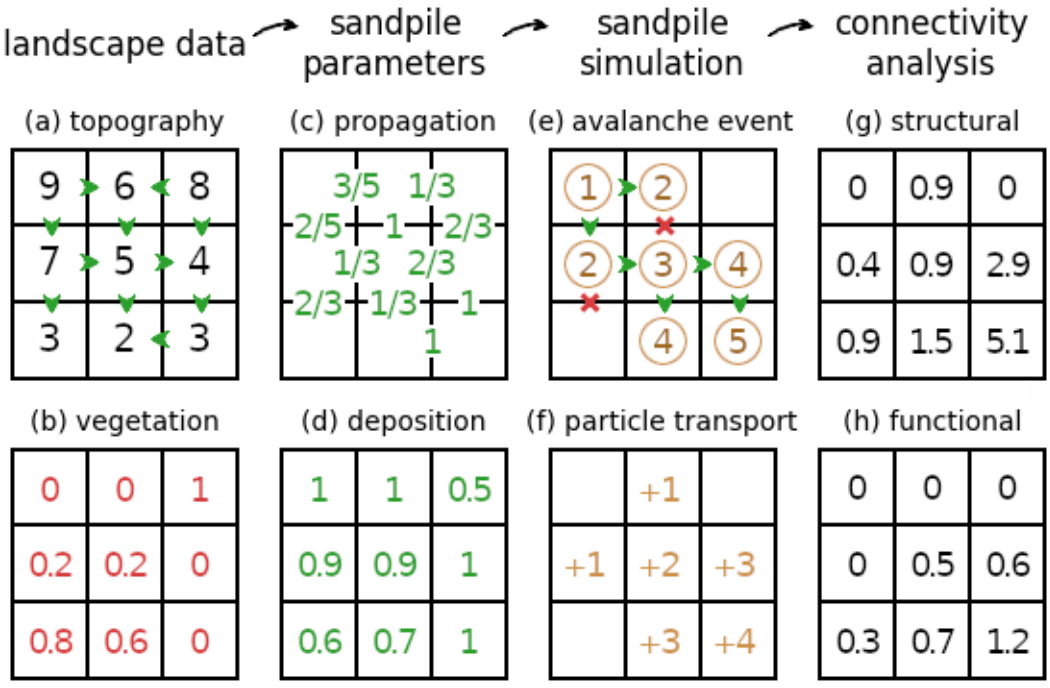


Figure 1. From landscape data to connectivity analysis in the case of a toy (3×3) **lattice.** The first column represents the *landscape data* comprised of **(a)** topography (elevation profile) and **(b)** vegetation density. The second column represents the *sandpile parameters* model the landscape considering **(c)** propagation probabilities (on links) depending on topography (see Section 2.1.2), and **(d)** deposition probabilities (on nodes). The third column illustrates five time steps of a *sandpile simulation* where **(e)** a single avalanche event of size $z = 6$ comprised of five topplings occurs. Integers refer to time steps, green arrows indicate particle propagation and deposition, and red crosses indicate particle propagation but non-deposition. The particle transport (length) occurring in (e) is recorded as in **(f)**. The fourth column portrays the *connectivity analysis*, which involves the computation of a **(g)** structural connectivity using only (c) as input (see Section 2.6.1) and measuring a **(h)** functional connectivity at the end of an entire sandpile simulation. In this example, the SC-FC Pearson correlation coefficient between (g) and (h) is equal to 0.9.

vegetation density denoted $v_i \in [0, 1]$ (static vegetation) and $A(i)$ the set of adjacent downslope nodes in its four-neighbourhood (in the four cardinal directions). We denote the out-degree of node i as $k_i = |A(i)|$: the number of downslope neighbouring nodes of i. k_i serves as the local toppling threshold, a static property derived directly from the topography that represents the critical local stress required to initiate sediment transport at that location. The sandpile model follows alternating *accumulation* and *relaxation* phases:

[label=(i)]

1. During the *accumulation* phase, at every time step t, a random node $i \in L$ is chosen and receives a particle with a probability $1 - \frac{v_i}{2}$.

https://doi.org/10.5194/egusphere-2026-6135
Preprint. Discussion started: 22 November 2026
© Author(s) 2026. CC BY 4.0 License.

Table 1. Simplified representation of hillslope erosion processes and controls within the sandpile model.

Natural phenomenon	Sandpile analogy
Local potential for soil mobilisation	Number of sand particles on a node.
Topographically-controlled sediment transport pathways	Directed links from high-elevation nodes to lower-elevation neighbouring nodes.
Rainfall event	One complete sandpile simulation.
Antecedent soil conditions	Initial distribution of particles on the lattice.
Rainfall and flow-driven detachment and mobilisation	Sediment accumulation phase during which particles are added to randomly chosen nodes, according to a uniform distribution.
Threshold for sediment transport	Toppling threshold of a node preceding an avalanche.
Runoff and sediment transport	Relaxation phase during which particles topple and are redistributed to lower-elevation neighbouring nodes.
Effect of vegetation on infiltration, surface resistance and sediment trapping	Nodes dissipate incoming particles in proportion to their local vegetation density.

2. The *relaxation* phase ensues if one node i is unstable, i.e., $s_i \geq k_i$ such that:

$$
\begin{aligned}
&s_i \rightarrow s_i - k_i \\
&s_j \rightarrow s_j + \delta_j, \forall j \in A(i) \\
&\text{with } \delta_j = \begin{cases} 1 & \text{with probability } 1 - \frac{v_j}{2} \\ 0 & \text{with probability } \frac{v_j}{2} \end{cases}.
\end{aligned} \tag{1}
$$

This process is repeated until $s_i < k_i$ for all $i \in L$ after which the *relaxation* phase ends and the *accumulation* phase restarts.

The redistribution of sediment over the hillslope plot is modelled according to either: (1) *probabilistic descent dynamics* where particles from i to $j \in A(i)$ in proportion to the elevation difference (see Section 2.1.2), or (2) *deterministic descent dynamics* where particles are transported entirely to the adjacent node with the lowest elevation, following the steepest descent flow routing used in MAHLERAN (see Section 2.1.3).

https://doi.org/10.5194/egusphere-2026-6135
Preprint. Discussion started: 22 November 2026
© Author(s) 2026. CC BY 4.0 License.

2.1.2 Probabilistic descent dynamics

During the *relaxation* phase of an unstable node $i \in G$, particles propagate to the successive $j \in A(i)$ with a probability equal to the *elevation difference* $e_{ij} = \begin{cases} \frac{e_j - e_i}{\overline{e_i}} & \text{if } e_j - e_i > 0 \\ 0 & \text{otherwise} \end{cases}$ where e_i is the elevation at node i and $\overline{e_i}$ a normalisation factor, such that $\sum_{j \in A(i)} e_{ij} = 1$. Then, as defined earlier, the algorithm (1) follows. This defines the *probabilistic* descent dynamics. Figure 1(c) provides an example of an avalanche event on a toy (3×3) lattice.

2.1.3 Deterministic descent dynamics

To compare the erosion patterns described by the sandpile model with those of MAHLERAN, we use a version of the sandpile model with deterministic descent dynamics, in which during the *relaxation* phase, particles propagate from i to its unique successor $j = \underset{k \in A(i)}{\text{argmin}}(e_k)$. This defines the *deterministic* descent dynamics.

2.2 Field data

2.2.1 Grassland and shrubland hillslope plots

The underlying topology and vegetation distributions used in the simulations are derived from grass-dominated and shrub-dominated $(30\,m \times 10\,m)$ hillslope plots at the Sevilleta Long Term Ecological Research site in central New Mexico, USA, for which we have rich field observational data Turnbull et al. (2010b). These hillslopes have also been extensively studied using MAHLERAN in Turnbull et al. (2010a). These $30\,m$ long plots represent segments of hillslopes that often extend from 300 to 500 meters in this landscape. They have been selected to illustrate the scale at which changes in hydrological and sediment connectivity are driven by vegetation patchiness, before gully formation becomes an increasingly important erosion process Bull and Kirkby (1997).

These grassland and shrubland plots are mapped onto (60×20) lattices where each of the $N = 60 \times 20 = 1200$ nodes represents a $0.5\,m$ grid: $\mathbb{G}$ represents a 43% covered grassland plot and $\mathbb{S}$ a 23% covered shrubland plot. These are respectively referred to as $\mathbb{G}$ and $\mathbb{S}$, the *empirical landscapes* of our study.

2.2.2 Rainfall data

We use nine rainfall events from Turnbull et al. (2010a): four on $\mathbb{G}$ and five on $\mathbb{S}$. Each event consists of a time series of varying duration and intensity, recorded minute by minute in mm/hr, see details in Table S1 in the supplementary material. In the sandpile model, we equate a unit of rainfall rate intensity r (mm/hr) with the addition of the rounded-up integer of r particles to the lattice during accumulation phases.

https://doi.org/10.5194/egusphere-2026-6135
Preprint. Discussion started: 22 November 2026
© Author(s) 2026. CC BY 4.0 License.

2.3 Evaluation against a process-based erosion model

To evaluate whether the sandpile model can replicate key erosion patterns captured by a detailed process-based model, we compare the sandpile model results to those simulated MAHLERAN (Model for Assessing Hillslope to Landscape Erosion, Runoff And Nutrients) Wainwright et al. (2008a, b, c), which is a process-based model designed to simulate runoff, soil erosion and nutrient transport at fine temporal and spatial resolutions, from individual hillslope plots to entire landscapes, capturing the dynamic interactions between rainfall intensity, soil erodibility, vegetation cover and microtopography. The model integrates runoff generation, flow routing (using a kinematic wave approximation), runon infiltration, splash erosion and flow-driven sediment detachment and transport. Sediment is predominantly transported downslope and deposited, depending on the local topography and flow conditions. MAHLERAN uses a steepest descent flow-routing algorithm, which directs water and sediment along the path of maximum slope.

MAHLERAN has been extensively validated in a range of dryland environments, including comparisons with field data on runoff, sediment export, spatial distribution of erosion and deposition patterns under varying environmental conditions Turnbull et al. (2012, 2010b); Wainwright et al. (2008c); Mueller et al. (2007a, b); Tatard et al. (2008). As a result, MAHLERAN has become a reliable tool for both research and practical applications, including identifying erosion hotspots, understanding sediment and nutrient redistribution, assessing the effectiveness of soil-conservation measures, and informing land-management strategies Okin et al. (2009); Turnbull et al. (2010b); Tiwari et al. (2025).

MAHLERAN has undergone extensive spatial verification beyond sediment export, including detailed testing of its hydraulics component using spatially distributed rainfall-simulation data on shrubland and grassland hillslopes Scoging et al. (1992); Parsons et al. (1997); Tatard et al. (2008); Wainwright et al. (2008c); Turnbull et al. (2010a). In addition, the model has been consistently evaluated against sediment fluxes rather than yields, demonstrating confidence in its representation of spatial erosion processes across scales Parsons et al. (2004, 2006a, b); Wainwright et al. (2008a). Further validation has used soil particle-size data to evaluate desert-pavement development Wainwright et al. (1999, 1995); Mueller et al. (2007a), and a Marker-in-Cell version of the model has successfully reproduced tracer distributions in rainfall-simulation experiments Cooper et al. (2012).

The application of MAHLERAN in this study uses a parameter set including rainfall characteristics (intensity and duration, or variability through time), a digital elevation model, soil texture and density, infiltration and roughness parameters, and vegetation and pavement cover.

In addition to direct comparisons with field observations of sediment exports, the two models are evaluated on the basis of the structural (SC) and functional connectivity (FC) patterns they describe, which together constitute what we refer to here as soil-erosion connectivity, a multidisciplinary conceptual framework used to analyse complex systems Turnbull et al. (2018); Voutsa et al. (2021); Sporns et al. (2005); Horn et al. (2014), with particularly rich precedents in geomorphology where functional connectivity encompasses both notions of hydrological and sediment connectivity Pöppl et al. (2025); Bracken et al. (2015); Bracken and Croke (2007); Lexartza-Artza and Wainwright (2009); Cavalli et al. (2013); Baartman et al. (2013), and which can help identify erosion hotspots Turnbull and Wainwright (2019). These two models are applied to dryland systems

https://doi.org/10.5194/egusphere-2026-6135
Preprint. Discussion started: 22 November 2026
© Author(s) 2026. CC BY 4.0 License.

characterised by resource scarcity and consequently, patchy vegetation covers Aguiar and Sala (1999), which leads to (and is in part created by) heterogeneous erosion patterns. Within this context, we focus on grasslands and shrublands, which together account for over half of the global dryland area (40.5% and 15.5%, respectively) according to MODIS land cover data Piao et al. (2024), highlighting their ecological relevance.

2.4 Sediment-export evaluation

To evaluate whether the sandpile model can reproduce the observed relationship between rainfall characteristics and event-scale sediment export, we use Spearman's rank correlation Spearman (1961) to assess the correspondence between rainfall and sediment export without assuming a specific functional relationship, as in Turnbull et al. Turnbull et al. (2010a).

For each sandpile model simulation, sediment export from the hillslope plot is quantified as the total number of particles leaving the lattice ($\mathbb{G}$ or $\mathbb{S}$) from its outflow boundary. Here, sediment export refers to the total mass of material transported downslope per rainfall event, expressed as event-based fluxes rather than area-normalised yields. As the sandpile model is scale-agnostic, the aim of this evaluation is not to test its capacity for predicting absolute sediment exports, but rather to replicate the recognised correlation between rainfall intensity (the input/stimulus) and sediment export (the output/response).

To allow for comparison between the different approaches, we apply an arbitrary scaling coefficient, whereby 200 exiting particles are equivalent to 1 kg of sediment export. This conversion has no mechanistic role in the model but provides a common unit to allow us to intuitively compare sandpile exports with field data and MAHLERAN simulation outputs.

2.5 Data generation

To understand how the distribution of vegetation affects erosion dynamics, we generate synthetic representations of grassland and shrubland hillslopes with varying vegetation density and vegetation-associated microtopographyParsons et al. (1997). This generation involves: (i) sampling vegetation density from the field data and distributing it across the lattice according to a given degree of clustering, and (ii) generating the appropriate microtopography based on the empirical relationship between vegetation and microtopography found on grassland and shrubland plots.

2.5.1 Vegetation clustering

Vegetation distributions over the lattice are generated as follows. Let $\mathbb{L}$ denote the lattice model of an empirical landscape, such as $\mathbb{G}$ or $\mathbb{S}$. L denotes the generated lattice derived from the empirical $\mathbb{L}$. Let $c \in [0, 1]$ denote the *vegetation cover* of L, i.e., the proportion of nodes with a non-zero vegetation density.

Similar to many other complex adaptive systems Juanico et al. (2005), vegetation in drylands tends not to be uniformly distributed and displays clustering Mueller et al. (2014). To distribute vegetation on L according to a clustering probability p_c, a node $i \in L$ is randomly chosen and a vegetation density $v_i > 0$ is assigned to it. v_i is sampled from the empirical distribution of non-zero vegetation densities of $\mathbb{L}$, as shown in Figure S1 in the supplementary material for $\mathbb{G}$ and $\mathbb{S}$.

https://doi.org/10.5194/egusphere-2026-6135
Preprint. Discussion started: 22 November 2026
© Author(s) 2026. CC BY 4.0 License.

Further, a non-vegetated node j (i.e. verifying $v_j = 0$) is chosen at random from $\begin{cases} \in A'(i) & \text{with probability } p_c \\ \notin A'(i) & \text{otherwise} \end{cases}$ where $A'(i)$ is the set of eight nodes surrounding i. This process is iterated until the chosen vegetation cover c is reached. Figure S2 in the supplementary material provides examples of vegetation plots of cover $c = 0.3$ for three clustering values $p_c = \{0.2, 0.5, 0.8\}$.

2.5.2 Microtopography

The elevation of each node i of the field data $\mathbb{L}$ is given by $e_i = E_i + \mu_i e_i$, where E_i is the *planar elevation* of i (i.e. the average elevation of all nodes in the same row as i) and μ_i represents *microtopography*. The following five steps summarise the algorithm used to generate microtopography for the generated L based on its vegetation distribution:

1. Compute a *surrounding vegetation density* score for each node $i \in \mathbb{L}$ as $w_i = v_i + \sum_{j \in A(i)} v_j + (4 - |A(i)|)\, v_i$ where v_i is the vegetation density of i and $A(i)$ is its four-neighbourhood. The correction term adjusts for boundary nodes to ensure that $w_i \in [0,5]$ for all $i \in \mathbb{L}$.

2. Fit a linear regression $y(x) = ax + b$ between node microtopography and corresponding scores, for both $\mathbb{G}$ (see Figure 2(a)) and $\mathbb{S}$ (see Figure 2(b)).

3. Compute w_i for each node $i \in L$ of the generated landscape.

4. Assign to each node $i \in L$ an elevation $e_i = E_i + a\, v_i + b + \sigma\eta$ where E_i uses the same planar elevation as $\mathbb{L}$. $\sigma = \sqrt{\frac{1}{N} \sum_{i \in \mathbb{L}} (\mu_i - y(v_i))^2}$ is the standard deviation between the linear regression line y and empirical microtopography μ. $\eta \in [-\sigma/2, \sigma/2]$ is a random number sampled from a uniform distribution introducing noise.

5. Correct sinks (nodes lower than all of its neighbours) by raising them to the height of their lowest neighbour by $\epsilon = 0.01$ to ensure uninterrupted particle flow.

Figure 2 illustrates the example of microtopography generated for $\mathbb{S}$.

2.6 Data analysis

Given the complexity of the lattice topology and the model dynamics, exact analytical solutions are intractable. For this reason, we perform extensive numerical experiments and analyse them by means of statistics.

To characterise erosion dynamics, each node is described by: (1) a *structural connectivity (SC)*, which assess potential sediment transport based on topography, and (2) a *functional connectivity (FC)*, which captures actual sediment transport during rainfall events. Here we follow the convention in connectivity science where SC reflects potential pathways defined by landscape structure, while FC reflects realised transport dynamics Bracken et al. (2013). We note that vegetation influences are expressed indirectly through their effect on microtopography and explicitly in the functional dynamics. Furthermore, each

https://doi.org/10.5194/egusphere-2026-6135
Preprint. Discussion started: 22 November 2026
© Author(s) 2026. CC BY 4.0 License.

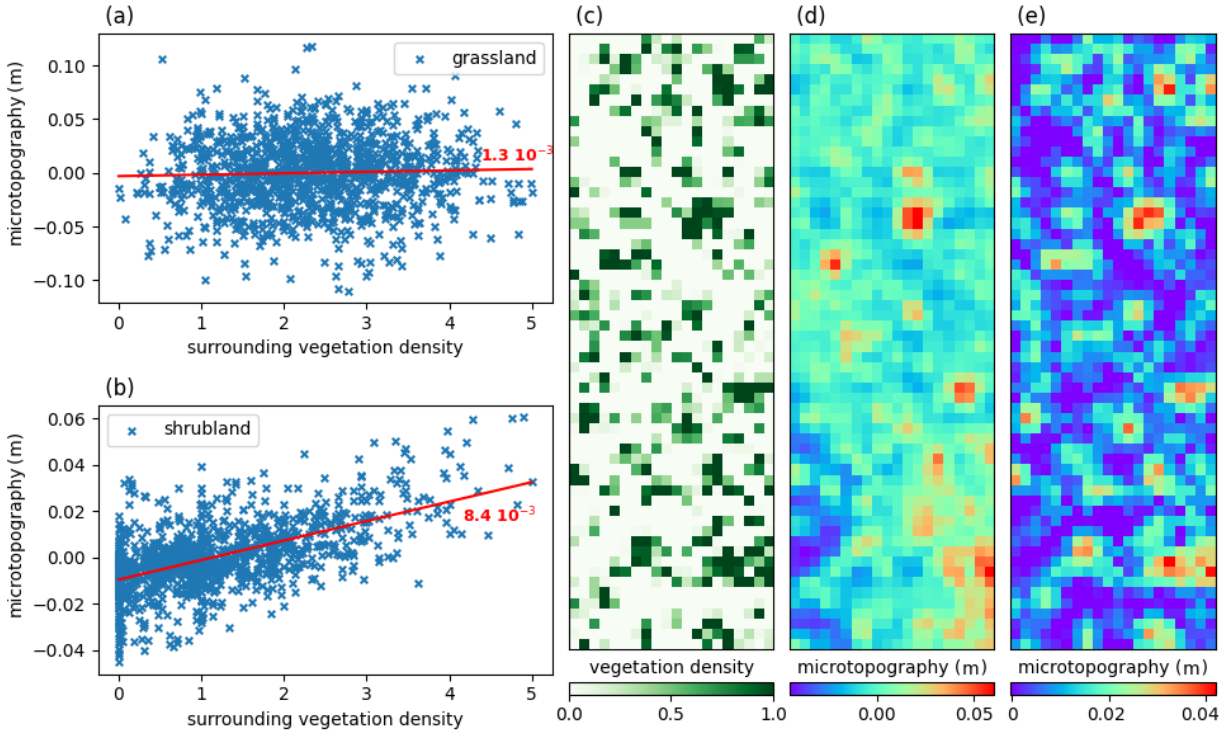


Figure 2. Data-driven topography generation algorithm. **(a)** Coupling strength between microtopography and surrounding vegetation density on grassland. The red line represents a linear regression between the two, with a slope of $a = 1.3 \times 10^{-3}$. **(b)** Coupling strength between microtopography and surrounding vegetation density on shrubland. The red line represents a linear regression between the two, with a slope of $b = 8.4 \times 10^{-3}$. **(c)** Vegetation density of the shrubland plot used in (b). **(d)** Microtopography (topography minus planar elevation) of the shrubland plot used in (b) and (c). **(e)** Reconstructed microtopography of the shrubland using as input the vegetation density from (c) and the linear regression (slope and standard deviation) from (b).

landscape is characterised by (3) a *SC-FC correlation* relating the two connectivity measures, and (4) an avalanche-size distribution.

2.6.1 Structural connectivity

The structural connectivity of a node i is defined as $SC(i) = \sum_{kl \in \mathcal{E}_i} e_{kl}$ where $\mathcal{E}_i$ is the set of edges forming paths towards i and ekl is the elevation difference between nodes k and l. Figure 1 illustrates this structural connectivity for a (3×3) lattice assuming *probabilistic* dynamics.

SC(i) evaluates the connectivity of the upslope area of i, serving as a proxy for potential particle deposition and highlighting paths or regions where erosion is most likely, based purely on topography. As such, it constitutes a slope-weighted version of flow accumulation Jenson and Domingue (1988).

https://doi.org/10.5194/egusphere-2026-6135
Preprint. Discussion started: 22 November 2026
© Author(s) 2026. CC BY 4.0 License.



2.6.2 Functional connectivity

The functional connectivity of FC(i) is the variance of the distances travelled by particles before depositing at i in a simulation. Figure 1(e-f) illustrates this functional connectivity for an avalanche event.

FC(i) captures actual transport patterns, incorporating vegetation and rainfall effects by tracking how far particles are transported before depositing in i.

2.6.3 SC-FC correlation

The *SC-FC correlation* ρ is the Pearson correlation coefficient (Benesty et al., 2009) between SC and FC. It is thus an indicator of the extent to which topography alone accounts for observed transport patterns: A high correlation signifies that topography is the dominant organising factor in shaping erosion pathways, while a lower correlation highlights the increasing role of vegetation and other processes in modifying these pathways.

2.6.4 Avalanche sizes: evaluating collective dynamics

The size of an avalanche is the total number of particles transported and deposited during the avalanche (e.g., an avalanche of size $z = 6$ in Figures 1(e) and 1(f)). Analysing the distributions of avalanche sizes enables characterisation of the system's collective dynamics. A heavier-tailed distribution suggests a landscape prone to extreme erosion events, which can drive large-scale biophysical changes and contribute to abrupt shifts in system state due to soil loss.

These distributions are fitted using the Python package powerlaw Alstott et al. (2014) and are found to be best described by exponentially truncated power laws. This is consistent with previous dissipative sandpile models Olami et al. (1992). The form of the distribution is given by $p(z) \propto z^{-\alpha} e^{-z/z_0}$, where α is the *scaling exponent* determining the power law slope for small sizes z, and z_0 is the *cut-off parameter* controlling the exponential decay for larger sizes z.

A smaller α (weaker slope) indicates a heavier-tailed distribution and more frequent large avalanches approaching the effective system size. A small z_0 (strict cut-off) indicates strong constraints on the largest avalanches. Conversely, a larger z_0 (loose cut-off) means that avalanches follow a pure power law over a wider range of values. Thus, α and z_0 capture different aspects of the heavy-tailedness, decreasing along α and increasing along z_0.

In practice, we find that avalanches of size $z = 1$ are under-represented compared to a power law (see Section 2.6.4), which can significantly bias the estimates of the scaling exponent α. Thus, we restrict the distribution fit to $z \geq 2$ which improves accuracy while capturing small avalanche scaling.

https://doi.org/10.5194/egusphere-2026-6135
Preprint. Discussion started: 22 November 2026
© Author(s) 2026. CC BY 4.0 License.

3 Results

3.1 Evaluating the sandpile model

3.1.1 SC-FC correlations

To evaluate whether our sandpile model captures the erosion patterns observed in MAHLERAN, we perform 100 simulations on $\mathbb{S}$ using deterministic descent dynamics over 10^4 time steps. Figure 3 presents the results, where the sandpile-derived FC is compared over time with both structural connectivity (SC) and MAHLERAN's sediment connectivity FC*, using the Pearson correlation coefficient. Figure 3(a) shows how FC converges consistently toward both SC and FC* saturating at an average correlation of 0.86 and 0.88, respectively. The spatial patterns associated with this convergence are illustrated in Figures 3(b-e), comparing vegetation density with SC, FC (after 10^4 time steps), and FC*. These experiments are replicated on $\mathbb{G}$, and the results are provided in Figure S3 in the supplementary material.

3.1.2 Sediment exports

For each of the nine rainfall events in Section 2.2.2, we run 50 simulations using deterministic descent dynamics. The average number of particles exiting the lattice is shown in Figure 4. Table 2 presents the Spearman correlation coefficients comparing empirical sediment exports with those from MAHLERAN and the sandpile model.

Figure 4 compares the sandpile sediment exports with MAHLERAN and field data for all nine rainfall events. Overall, the sandpile model reproduces the relationship between rainfall amount and sediment exports found empirically and predicted by MAHLERAN, except for the largest rainfall events on shrubland (05.07.06 and 07.09.06), where discrepancies arise and exports are underestimated.

Table 2. Pairwise Spearman's rank correlation coefficients between the sediment exports monitored empirically, modeled by MAHLERAN and the sandpile model, on either grassland (four rainfall events), shrubland (five rainfall events) or both (nine rainfall events).

Spearman correlation between	on grassland	on shrubland	on both
Monitored and MAHLERAN data	0.95	1	0.88
Monitored and sandpile data	0.95	0.60	0.78
Sandpile and MAHLERAN data	1	0.60	0.83

3.2 Exploration

Having compared our sandpile model with MAHLERAN and empirical data, we now lift the deterministic descent approximation in favor of the more general *probabilistic* descent dynamics. This flexibility allows us to investigate how vegetation and topography shape erosion dynamics in both empirical and generated landscapes.

https://doi.org/10.5194/egusphere-2026-6135
Preprint. Discussion started: 22 November 2026
© Author(s) 2026. CC BY 4.0 License.



3.2.1 On empirical landscapes: exploring probabilistic descent dynamics

We run 100 simulations of 5×10^5 time steps on both $\mathbb{G}$ and $\mathbb{S}$, with results shown in Figure 5. As shown in Figure5 (a), FC converges consistently to SC, regardless of the descent dynamics used. However, this convergence is much slower under probabilistic descent dynamics than under the deterministic approximation. The average final steady-state SC-FC correlation is equal to $\rho^{\mathbb{G}} = 0.53$ on grassland and $\rho^{\mathbb{S}} = 0.74$ on shrubland.

Figure 5(b) compares avalanche size distributions in grassland $\mathbb{G}$ and shrubland $\mathbb{S}$. $\mathbb{S}$ exhibits significantly larger avalanches than $\mathbb{G}$, as indicated by their scaling coefficients ($\alpha^{\mathbb{S}} = 1.35 < \alpha^{\mathbb{G}} = 1.73$), suggesting more potential for system-wide geomorphic feedback in the former.

Although the cut-off parameters differ, both remain much smaller than one ($z_0^{\mathbb{S}} = 0.013 < z_0^{\mathbb{G}} = 0.037 \ll 1$), indicating strong constraints on the largest avalanches. We therefore use the scaling exponent α as the primary measure of differences in tail heaviness.

Shrub encroachment is often linked to *xerification* (loss of vegetation density, see Figures 5(c) and 5(f)). In fact, in our empirical landscapes, $\mathbb{G}$ has 954 vegetated nodes, which is a vegetation cover of $c^{\mathbb{G}} = \dfrac{954}{1200} \approx 0.8$ and a total density of $\sum_{i \in \mathbb{G}} v_i = 556.6$. In contrast, $\mathbb{S}$ has 493 vegetated nodes, which is a vegetation cover of $c^{\mathbb{S}} = \dfrac{493}{1200} \approx 0.4$, and a total density of $\sum_{i \in \mathbb{S}} v_i = 274.9$. Therefore, it remains unclear whether the larger avalanches in $\mathbb{S}$ result from the impact of shrub encroachment on flow pathways or from the reduced dissipation that comes with xerification. The next section disentangles these effects.

3.2.2 Vegetation-topography interactions on generated landscapes

We generate 100 different (60×20) lattices L_i^p for three different vegetation clustering probabilities $p_c = \{0.2, 0.5, 0.8\}$ with a vegetation cover $c = 0.3$. Vegetation densities are randomly sampled from the distribution of non-zero vegetation on $\mathbb{S}$. Note that sampling vegetation density from $\mathbb{S}$ or $\mathbb{G}$ (see the distribution of vegetation density for comparison in Figure S1 of the supplementary material) or even binarising it ($v_i = 0, 1$ for all $i \in G$) does not qualitatively affect our results (not shown here).

For each lattice, we assume vegetation to be either grass or shrub and generate its topography accordingly, as described in Section 2.5.2. In each case, we run 100 simulations considering probabilistic descent dynamics for 10^5 time steps.

Figure 6 illustrates the relationship between avalanche size distribution heavy-tailedness and SC-FC correlations (erosion hotspot predictability) across generated grasslands and shrublands with varying clustering probabilities.

Here, the trend is reversed: Generated grasslands exhibit larger avalanches than generated shrublands. On average, the scaling exponents observed on grasslands are smaller than those observed on shrublands ($\overline{\alpha}^G = 1.38 < \overline{\alpha}^S = 1.56$). As with their empirical counterparts, cut-off parameters are always much smaller than one ($\overline{z}_0^S = 0.016 < \overline{z}_0^G = 0.024 \ll 1$). SC-FC correlations are larger on grasslands than on shrublands ($\overline{\rho}^G = 0.63 > \overline{\rho}^S = 0.58$).

For the same landscape type, the mean and standard deviation of each of the parameters α, z_0 and ρ do not appear to be affected by vegetation clustering. These values are reported in detail in Tables S2 and S3 of the supplementary material, for the means and standard deviations, respectively.

https://doi.org/10.5194/egusphere-2026-6135
Preprint. Discussion started: 22 November 2026
© Author(s) 2026. CC BY 4.0 License.

4 Discussion

We have demonstrated how a minimal sandpile model can effectively reproduce sediment export observed in field settings, as well as erosion patterns described by MAHLERAN, thus highlighting the applicability across diverse patchy landscapes. The sandpile model generally reproduces observed trends (see Figure 4), except for extreme rainfall events exceeding 4 kg sediment export. This discrepancy stems from the model's simplifications: (i) Particle transport is assumed to occur from a single point at a time, overlooking the cumulative effects of pathway concentration. (ii) The model is not simulating rainfall intensity per se, but only modulating its duration. (iii) The process is memory-free, as erosion does not progressively alter soil conditions. Specifically, the lack of memory prevents the model from capturing the non-linear runaway effects of rill development and soil saturation that typically amplify sediment yield during high-impact events. These simplifications, which do not account for non-linear hydrological processes and evolving soil properties, lead to larger discrepancies under extreme rainfall Durighetto et al. (2022); Crave and Davy (2001). Whether this trade-off between simplicity and precision is acceptable ultimately depends on the intended application context.

In terms of the spatial patterns which we assessed using connectivity metrics, we found that the functional connectivity (FC) from the sandpile model consistently converges to the functional connectivity (FC*) from MAHLERAN. Both are well approximated by the introduced structural connectivity (SC), hence, enabling erosion hotspot identification from topography alone in data-limited settings. SC-FC correlations are stronger in shrubland than in grassland (Figure 3), likely due to vegetation loss in shrubland causing dynamics to follow topography more closely. Thus, SC emerges as a reliable and computationally efficient predictor of erosion hotspots in shrub-encroached areas.

The avalanche-size distributions analyses provide further insight into the landscape-scale geomorphic responses. We find that shrublands exhibit significantly larger erosion events than grasslands, as indicated by their scaling exponents: $\alpha^{(\mathbb{S})} = 1.35$ for shrubland and $\alpha^{(\mathbb{G})} = 1.73$ for grassland. However, the difference in cutoff parameters ($z_0^{(\mathbb{S})} = 0.013 < z_0^{(\mathbb{G})} = 0.037$) is too small to suggest a difference in heavy-tailedness. In fact, both distributions have a very small cutoff ($z_0 \ll 1$) indicating strong constraints on large avalanches, likely imposed by the lattice structure (topography) rather than by dissipation patterns (vegetation) Yadav et al. (2022).

However, this comparison alone is insufficient to fully clarify how vegetation type, distribution, (total) cover, and (local) density influence soil erosion. To achieve this, a data-driven algorithm is developed to capture the empirical relationship between local vegetation density and microtopography in grassland and shrubland Turnbull et al. (2010b) and which is then used to generate multiple landscapes controlling for these four confounding factors. Vegetation cover and density per node (i.e. total system dissipation) are set to arbitrary values. The two remaining factors, shrub encroachment (shrubland vs. grassland) and vegetation clustering, are varied to assess their impact on system-wide geomorphic feedback (frequency of large avalanches).

Grassland microtopography is found to be weakly related to vegetation density, unlike in shrubland, where this relationship is positive. Accordingly, grassland is used as a control, while shrubland is used to investigate the role of vegetation-microtopography coupling in emergent collective dynamics, as characterised by the observed connectivity patterns and event-size distributions. Comparing the generated and empirical grassland landscapes, we observe an increase in both SC-FC correla-

https://doi.org/10.5194/egusphere-2026-6135
Preprint. Discussion started: 22 November 2026
© Author(s) 2026. CC BY 4.0 License.

tions ($\rho^{\mathbb{G}} = 0.54 < \overline{\rho}^{G} = 0.63$) and heavy-tailedness of the event-size distribution, as indicated by the lower scaling exponent ($\alpha^{\mathbb{G}} = 1.73 > \overline{\alpha}^{G} = 1.38$). These changes are consistent with the substantial decrease in vegetation cover, from $c^{\mathbb{G}} = 0.8$ to $c^{G} = 0.3$, as weaker dissipation allows: (i) particles to continue along topographic connections without being dissipated, increasing SC-FC correlation, and (ii) larger avalanches to occur.

At matched vegetation cover and dissipation, the stronger shrubland coupling produces lower SC-FC correlations ($\overline{\rho}^{S} = 0.58 < \overline{\rho}^{G} = 0.63$) and less heavy-tailed event-size distributions ($\overline{\alpha}^{S} = 1.56 > \overline{\alpha}^{S} = 1.38$) than grassland. This suggests that, in shrubland, vegetation-microtopography coupling introduces an effect opposite to that of weaker dissipation alone, strong enough to reverse the response observed in grassland. One possible explanation is that the stronger microtopographic perturbations generated in shrubland increase local routing complexity, making the topography-based SC less representative of the dynamically realised transport (FC), while also interrupting larger avalanches. At larger scales, such interruption could arise from percolation-like vegetation configurations in the transverse direction of the hillslope, causing pathway fragmentation.

The same reversal is observed when comparing empirical and generated shrubland, where lower vegetation cover (from $c^{\mathbb{S}} = 0.4$ to $c^{S} = 0.3$) is again associated with a lower SC-FC correlation and lower heavy-tailedness. However, this comparison involves a single empirical landscape and therefore provides weaker statistical support. More generally, vegetation-associated microtopography is known to reorganise flow through local convergence and divergence around shrubs Howes and Abrahams (2003); Turnbull and Wainwright (2019). Our results suggest that this coupling affects not only local flow pathways, but also system-level outcomes captured by SC-FC correlations and the avalanche-size distribution.

For each of α, z_0 and ρ, the variability among generated landscapes is comparable to the difference between the grassland and shrubland mean values, regardless of the clustering probability used. Thus, while clustering is retained as a realistic feature of vegetation distribution, it does not emerge as a control parameter for the collective dynamics within the range tested.

Taken together, these results point to vegetation-microtopography coupling as the dominant control on the large-scale collective response in the generated landscapes, with vegetation loss alone producing a secondary effect Turnbull and Wainwright (2019); Tiwari et al. (2025).

Across both generated landscape types and regardless of vegetation clustering, ρ is inversely related to α, see the slope of the linear regressions (red lines) in Figure 6, notably, the Pearson correlation between ρ and α is ≈ 0.6. This indicates that the proposed topography-based SC measure is a more reliable predictor of erosion hotspots in landscapes where large avalanches are more frequent and thus, on landscapes that are more prone to large-scale geomorphic feedback.

Here, vegetation density and microtopography are positively correlated in shrublands but largely uncorrelated in grasslands. However, such relationships are not universal, many deep-rooted grasses are known to stabilise soil and trap sediment, mitigating erosion Kumarasinghe (2021); Pan and Ma (2020). Therefore, the applicability of our findings regarding these specific vegetation-topography correlations is primarily within the ecological and regional contexts of our field data, and should not be overgeneralised to other systems. Moreover, extending the model to other arid systems would require re-evaluating vegetation-topography relationships and validating it against system-specific data.

https://doi.org/10.5194/egusphere-2026-6135
Preprint. Discussion started: 22 November 2026
© Author(s) 2026. CC BY 4.0 License.

5 Conclusions

Our results highlight pathway complexity as a key organising factor in erosion patterns, while recognising that vegetation influences erosion through multiple hydrological (e.g. increasing infiltration rates) and geomorphic (e.g. increasing surface roughness and providing root reinforcement that stabilise soil) mechanisms that go beyond topographic modification. These processes are not explicitly captured in our minimal sandpile model. Nevertheless, the model successfully reproduces the large-scale patterns captured by a detailed process-based framework, showing that such simplification can be powerful for identifying erosion hotspots, even if it is not suitable for describing detailed biophysical feedback or predicting soil loss. This finding holds at the scale studied, but longer timescales introduce additional factors that shape landforms and alter flow pathways, including vegetation responses to water Parsons et al. (2004); Favis-Mortlock and Mullan (2011) and wind erosion Skidmore (2017); Shao (2008), landform evolution Marston (2010); Amundson et al. (2015), and external disturbances such as anthropogenic activity Reusser et al. (2015); Brown et al. (2017) and wildfire McGuire et al. (2024); Noske et al. (2024); Moody et al. (2013).

Despite its simplicity, the sandpile model captures key erosion dynamics and the intricate spatial patterns of erosion across hillslopes with contrasting vegetation distributions. These findings show that important aspects of dryland erosion dynamics can emerge from a minimal set of local threshold and redistribution rules, and that the coupling between vegetation distribution and microtopography, rather than vegetation cover alone, controls the organisation of transport pathways. The sandpile framework therefore provides a computationally efficient means of investigating the mechanisms that generate emergent erosion patterns, particularly where data for detailed parameterisation are limited. While our study focuses on drylands, the principles of connectivity-driven erosion apply broadly. Studies in mountainous catchments Heckmann and Schwanghart (2013), post-wildfire landscapes Robichaud et al. (2013), agricultural terrains Baartman et al. (2013), and coastal dune systems Delgado-Fernandez and Davidson-Arnott (2011) highlight the universal role of sediment connectivity in shaping erosion patterns. Our framework could be extended to these environments to explore how topography and vegetation regulate sediment transport under diverse hydrological and geomorphic conditions.

Code and data availability. The data and code samples used to simulate the sandpile model in this research project can be found at: https://github.com/Hajali-Selim/sandpile-erosion-connectivity. The MAHLERAN source code can be found at: https://github.com/john-wainwright/Mahleran_v1.2.3. For demonstration purposes, we also provide a lightweight interactive app for visualising empirical and generated landscapes, available at https://hillslope-connectivity-calculator.streamlit.app/.

Author contributions. S.H.A. and L.T. conceived the project; S.H.A. developed the methodology and software, performed the validation, formal analysis, and investigation, and created the visualisations; S.H.A. and L.T. curated the data; L.T., M.-T.H., and J.W. acquired funding; L.T. and M.-T.H. supervised the project; S.H.A. wrote the original draft; S.H.A., L.T., S.T., and J.W. reviewed and edited the manuscript.

https://doi.org/10.5194/egusphere-2026-6135
Preprint. Discussion started: 22 November 2026
© Author(s) 2026. CC BY 4.0 License.

Competing interests. The authors declare that they have no competing interests.

Acknowledgements. **Funding**

This project was funded by the European Union's Horizon 2020 research and innovation programme under the Marie Skłodowska-Curie grant agreement No. 859937. We also acknowledge support from the Sevilleta LTER funded by the National Science Foundation under grant agreement No. 1655499.

https://doi.org/10.5194/egusphere-2026-6135
Preprint. Discussion started: 22 November 2026
© Author(s) 2026. CC BY 4.0 License.

References

Aguiar, M. R. and Sala, O. E.: Patch structure, dynamics and implications for the functioning of arid ecosystems, Trends in Ecology & Evolution, 14, 273–277, https://doi.org/10.1016/S0169-5347(99)01612-2, 1999.

Aho, K., Kriloff, C., Godsey, S. E., Ramos, R., Wheeler, C., You, Y., Warix, S., Derryberry, D., Zipper, S., Hale, R. L., et al.: Non-perennial stream networks as directed acyclic graphs: The R-package streamDAG, Environmental Modelling & Software, 167, 105 775, https://doi.org/10.1016/j.envsoft.2023.105775, 2023.

Alstott, J., Bullmore, E., and Plenz, D.: powerlaw: a Python package for analysis of heavy-tailed distributions, PloS one, 9, e85 777, https://doi.org/10.1371/journal.pone.0085777, 2014.

Amundson, R., Heimsath, A., Owen, J., Yoo, K., and Dietrich, W. E.: Hillslope soils and vegetation, Geomorphology, 234, 122–132, https://doi.org/10.1016/j.geomorph.2014.12.031, 2015.

Baartman, J. E., Masselink, R., Keesstra, S. D., and Temme, A. J.: Linking landscape morphological complexity and sediment connectivity, Earth Surface Processes and Landforms, 38, 1457–1471, https://doi.org/10.1002/esp.3434, 2013.

Baartman, J. E., Nunes, J. P., Masselink, R., Darboux, F., Bielders, C., Degré, A., Cantreul, V., Cerdan, O., Grangeon, T., Fiener, P., et al.: What do models tell us about water and sediment connectivity?, Geomorphology, 367, 107 300, https://doi.org/10.1016/j.geomorph.2020.107300, 2020.

Bak, P., Tang, C., and Wiesenfeld, K.: Self-organized criticality, Physical Review A, 38, 364, https://doi.org/10.1103/PhysRevA.38.364, 1988.

Batterman, R. W.: Asymptotics and the role of minimal models, The British Journal for the Philosophy of Science, 53, 21–38, https://doi.org/10.1093/bjps/53.1.21, 2002.

Benesty, J., Chen, J., Huang, Y., and Cohen, I.: Pearson correlation coefficient, in: Noise reduction in speech processing, pp. 1–4, Springer, https://doi.org/10.1007/978-3-642-00296-0_5, 2009.

Bennett, N. D., Croke, B. F., Guariso, G., Guillaume, J. H., Hamilton, S. H., Jakeman, A. J., Marsili-Libelli, S., Newham, L. T., Norton, J. P., Perrin, C., et al.: Characterising performance of environmental models, Environmental Modelling & Software, 40, 1–20, https://doi.org/10.1016/j.envsoft.2012.09.011, 2013.

Borrelli, P., Alewell, C., Alvarez, P., Anache, J. A. A., Baartman, J., Ballabio, C., Bezak, N., Biddoccu, M., Cerdà, A., Chalise, D., et al.: Soil erosion modelling: A global review and statistical analysis, Science of the Total Environment, 780, 146 494, https://doi.org/10.1016/j.scitotenv.2021.146494, 2021.

Bout, V. and Jetten, V.: The validity of flow approximations when simulating catchment-integrated flash floods, Journal of Hydrology, 556, 674–688, https://doi.org/10.1016/j.jhydrol.2017.11.033, 2018.

Bracken, L., Wainwright, J., Ali, G., Tetzlaff, D., Smith, M., Reaney, S., and Roy, A.: Concepts of hydrological connectivity: Research approaches, pathways and future agendas, Earth-Science Reviews, 119, 17–34, https://doi.org/10.1016/j.earscirev.2013.02.001, 2013.

Bracken, L., Turnbull, L., Wainwright, J., and Bogaart, P.: Sediment connectivity: A framework for understanding sediment transfer at multiple scales, Earth Surface Processes and Landforms, 40, https://doi.org/10.1002/esp.3635, 2015.

Bracken, L. J. and Croke, J.: The concept of hydrological connectivity and its contribution to understanding runoff-dominated geomorphic systems, Hydrological Processes: An International Journal, 21, 1749–1763, https://doi.org/10.1002/hyp.6313, 2007.

https://doi.org/10.5194/egusphere-2026-6135
Preprint. Discussion started: 22 November 2026
© Author(s) 2026. CC BY 4.0 License.

Brown, A. G., Tooth, S., Bullard, J. E., Thomas, D. S., Chiverrell, R. C., Plater, A. J., Murton, J., Thorndycraft, V. R., Tarolli, P., Rose, J., et al.: The geomorphology of the Anthropocene: emergence, status and implications, Earth Surface Processes and Landforms, 42, 71–90, https://doi.org/10.1002/esp.3943, 2017.

Bull, L. and Kirkby, M.: Gully processes and modelling, Progress in physical geography, 21, 354–374, https://doi.org/10.1177/030913339702100302, 1997.

Cavalli, M., Trevisani, S., Comiti, F., and Marchi, L.: Geomorphometric assessment of spatial sediment connectivity in small Alpine catchments, Geomorphology, 188, 31–41, https://doi.org/10.1016/j.geomorph.2012.05.007, 2013.

Ciampalini, R., Follain, S., and Le Bissonnais, Y.: LandSoil: A model for analysing the impact of erosion on agricultural landscape evolution, Geomorphology, 175, 25–37, https://doi.org/10.1016/j.geomorph.2012.06.014, 2012.

Cooper, J. R., Wainwright, J., Parsons, A. J., Onda, Y., Fukuwara, T., Obana, E., Kitchener, B., Long, E. J., and Hargrave, G. H.: A new approach for simulating the redistribution of soil particles by water erosion: A marker-in-cell model, Journal of Geophysical Research: Earth Surface, 117, https://doi.org/10.1029/2012JF002499, 2012.

Cossart, É. and Fressard, M.: Assessment of structural sediment connectivity within catchments: insights from graph theory, Earth Surface Dynamics, 5, 253–268, https://doi.org/10.5194/esurf-5-253-2017, 2017.

Crave, A. and Davy, P.: A stochastic "precipiton" model for simulating erosion/sedimentation dynamics, Computers & Geosciences, 27, 815–827, https://doi.org/10.1016/S0098-3004(00)00167-9, 2001.

Delestre, O., Darboux, F., James, F., Lucas, C., Laguerre, C., and Cordier, S.: FullSWOF: full shallow-water equations for overland flow. J Open Source Softw 2 (20): 448, https://doi.org/10.21105/joss.00448, 2017.

Delgado-Fernandez, I. and Davidson-Arnott, R.: Meso-scale aeolian sediment input to coastal dunes: The nature of aeolian transport events, Geomorphology, 126, 217–232, https://doi.org/10.1016/j.geomorph.2011.04.001, 2011.

Devitt, L., Neal, J., Wagener, T., and Coxon, G.: Uncertainty in the extreme flood magnitude estimates of large-scale flood hazard models, Environmental Research Letters, 16, 064 013, https://doi.org/10.1088/1748-9326/abfac4, 2021.

Dhar, D. and Ramaswamy, R.: Exactly solved model of self-organized critical phenomena, Physical Review Letters, 63, 1659, https://doi.org/10.1103/PhysRevLett.63.1659, 1989.

Diodato, N.: Spatial uncertainty modeling of climate processes for extreme hydrogeomorphological events hazard monitoring, Journal of Environmental Engineering, 132, 1530–1538, https://ascelibrary.org/journal/jedegc, 2006.

Durighetto, N., Bertassello, L. E., and Botter, G.: Eco-hydrological modelling of channel network dynamics—Part 1: Stochastic simulation of active stream expansion and retraction, Royal Society Open Science, 9, 220 944, https://doi.org/10.1098/rsos.220944, 2022.

Favis-Mortlock, D. and Mullan, D.: Soil erosion by water under future climate change., in: Soil hydrology, land use and agriculture: measurement and modelling, pp. 384–414, CAB International Wallingford UK, https://www.cabidigitallibrary.org/, 2011.

Food and Agriculture Organization of the United Nations, ed.: Proceedings of the Global Symposium on Soil Erosion 2019: "Stop Soil Erosion, Save Our Future", FAO, Rome, Italy, https://www.fao.org/about/meetings/soil-erosion-symposium/resources/publications/en/, accessed: 2025-03-05, 2020.

Food and Agriculture Organization of the United Nations and Intergovernmental Technical Panel on Soils: Status of the World's Soil Resources: Main Report, FAO, Rome, Italy, https://www.fao.org/3/i5199e/i5199e.pdf, accessed: 2025-03-05, 2015.

Goldenfeld, N.: Lectures on phase transitions and the renormalization group, CRC Press, https://www.routledge.com/Lectures-on-Phase-Transitions-and-the-Renormalization-Group/Goldenfeld/p/book/9780201554090, 2018.

https://doi.org/10.5194/egusphere-2026-6135
Preprint. Discussion started: 22 November 2026
© Author(s) 2026. CC BY 4.0 License.

Govers, G., Vandaele, K., Desmet, P., Poesen, J., and Bunte, K.: The role of tillage in soil redistribution on hillslopes, European Journal of Soil Science, 45, 469–478, https://doi.org/10.1111/j.1365-2389.1994.tb00532.x, 1994.

Heckmann, T. and Schwanghart, W.: Geomorphic coupling and sediment connectivity in an alpine catchment—Exploring sediment cascades using graph theory, Geomorphology, 182, 89–103, https://doi.org/10.1016/j.geomorph.2012.10.033, 2013.

Horn, A., Ostwald, D., Reisert, M., and Blankenburg, F.: The structural–functional connectome and the default mode network of the human brain, Neuroimage, 102, 142–151, https://doi.org/10.1016/j.neuroimage.2013.09.069, 2014.

Howes, D. A. and Abrahams, A. D.: Modeling runoff and runon in a desert shrubland ecosystem, Jornada Basin, New Mexico, Geomorphology, 53, 45–73, https://doi.org/10.1016/S0169-555X(02)00347-1, 2003.

Jakeman, A. and Hornberger, G.: How much complexity is warranted in a rainfall-runoff model?, Water Resources Research, 29, 2637–2649, https://doi.org/10.1029/93WR00877, 1993.

Jenson, S. K. and Domingue, J. O.: Extracting topographic structure from digital elevation data for geographic information system analysis, Photogrammetric engineering and remote sensing, 54, 1593–1600, https://pubs.usgs.gov/publication/70142175, 1988.

Juanico, D. E., Monterola, C., and Saloma, C.: Cluster formation by allelomimesis in real-world complex adaptive systems, Physical Review E, 71, 041 905, https://doi.org/10.1103/PhysRevE.71.041905, 2005.

Kirkby, M. J.: A role for theoretical models in geomorphology?, in: The scientific nature of geomorphology: Proceedings of the 27th Binghamton Symposium in Geomorphology, vol. 27, p. 257, John Wiley & Sons, https://search.worldcat.org/search?q=The+scientific+nature+of+geomorphology+Proceedings+of+the+27th+Binghamton+Symposium+in+Geomorphology, 1996.

Kumarasinghe, U.: A review on new technologies in soil erosion management, J. Res. Technol. Eng, 2, 120–127, https://jrteng.com/, 2021.

Landemaine, V.: Érosion des sols et transferts sédimentaires sur les bassins versants de l'Ouest du Bassin de Paris: analyse, quantification et modélisation à l'échelle pluriannuelle, University of Rouen, https://theses.fr/?q=%C3%89rosion%20des%20sols%20et%20transferts%20s%C3%A9dimentaires%20sur%20les%20bassins%20versants%20de%20l%E2%80%99Ouest%20du%20Bassin%20de%20Paris, 2016.

Lexartza-Artza, I. and Wainwright, J.: Hydrological connectivity: Linking concepts with practical implications, Catena, 79, 146–152, https://doi.org/10.1016/j.catena.2009.07.001, 2009.

Manna, S. S.: Two-state model of self-organized criticality, Journal of Physics A: Mathematical and General, 24, L363, https://doi.org/10.1088/0305-4470/24/7/001, 1991.

Marston, R. A.: Geomorphology and vegetation on hillslopes: Interactions, dependencies, and feedback loops, Geomorphology, 116, 206–217, https://doi.org/10.1016/j.geomorph.2009.09.028, 2010.

Matteo, B., Guercio, R., Magini, R., et al.: A physically-based approach for evaluating the hydraulic invariance in urban transformations, International Journal of Safety and Security Engineering, 8, 536–546, https://doi.org/10.2495/SAFE-V8-N4-536-546, 2018.

McGuire, L. A., Ebel, B. A., Rengers, F. K., Vieira, D. C., and Nyman, P.: Fire effects on geomorphic processes, Nature Reviews Earth & Environment, 5, 486–503, https://doi.org/10.1038/s43017-024-00557-7, 2024.

Moody, J. A., Shakesby, R. A., Robichaud, P. R., Cannon, S. H., and Martin, D. A.: Current research issues related to post-wildfire runoff and erosion processes, Earth-Science Reviews, 122, 10–37, https://doi.org/10.1016/j.earscirev.2013.03.004, 2013.

Mueller, E. N., Wainwright, J., and Parsons, A. J.: Impact of connectivity on the modeling of overland flow within semiarid shrubland environments, Water Resources Research, 43, 2007a., https://doi.org/10.1029/2006WR005006.

Mueller, E. N., Wainwright, J., and Parsons, A. J.: The stability of vegetation boundaries and the propagation of desertification in the American Southwest: A modelling approach, Ecological Modelling, 208, 91–101, 2007b., https://doi.org/10.1016/j.ecolmodel.2007.04.010.

https://doi.org/10.5194/egusphere-2026-6135
Preprint. Discussion started: 22 November 2026
© Author(s) 2026. CC BY 4.0 License.



Mueller, E. N., Wainwright, J., Parsons, A. J., and Turnbull, L.: Patterns of land degradation in drylands, Dor-drecht: Springer, https://link.springer.com/search?query=Patterns+of+land+degradation+in+drylands+Mueller+Wainwright+Parsons+Turnbull, 2014.

Noske, P. J., Nyman, P., Lane, P. N., Rengers, F. K., and Sheridan, G. J.: Changes in soil erosion caused by wildfire: A conceptual biogeographic model, Geomorphology, p. 109272, https://doi.org/10.1016/j.geomorph.2024.109272, 2024.

Okin, G. S., Parsons, A. J., Wainwright, J., Herrick, J. E., Bestelmeyer, B. T., Peters, D. C., and Fredrickson, E. L.: Do changes in connectivity explain desertification?, BioScience, 59, 237–244, https://doi.org/10.1525/bio.2009.59.3.8, 2009.

Olami, Z., Feder, H. J. S., and Christensen, K.: Self-organized criticality in a continuous, nonconservative cellular automaton modeling earthquakes, Physical Review Letters, 68, 1244, https://doi.org/10.1103/PhysRevLett.68.1244, 1992.

Pan, C. and Ma, L.: How the spatial distribution of grass contributes to controlling hillslope erosion, Hydrological Processes, 34, 68–81, https://doi.org/10.1002/hyp.13742, 2020.

Parsons, A. J., Wainwright, J., Abrahams, A. D., and Simanton, J. R.: Distributed dynamic modelling of interrill overland flow, Hydrological Processes, 11, 1833–1859, https://doi.org/10.1002/(SICI)1099-1085(199712)11:15<1833::AID-HYP546>3.0.CO;2-7, 1997.

Parsons, A. J., Wainwright, J., Mark Powell, D., Kaduk, J., and Brazier, R. E.: A conceptual model for determining soil erosion by water, Earth Surface Processes and Landforms, 29, 1293–1302, https://doi.org/10.1002/esp.1096, 2004.

Parsons, A. J., Brazier, R. E., Wainwright, J., and Powell, D. M.: Scale relationships in hillslope runoff and erosion, Earth Surface Processes and Landforms: The Journal of the British Geomorphological Research Group, 31, 1384–1393, 2006a, https://doi.org/10.1002/esp.1345.

Parsons, A. J., Wainwright, J., Brazier, R. E., and Powell, D. M.: Is sediment delivery a fallacy?, Earth Surface Processes and Landforms, 2006b, https://doi.org/10.1002/esp.1395.

Piao, S., Zhang, Y., Zhu, Z., Lian, X., Huang, K., He, M., Zhao, C., and Liu, D.: Socioeconomic and Environmental Changes in Global Drylands, Dryland Social-Ecological Systems in Changing Environments, pp. 161–201, https://link.springer.com/search?query=Socioeconomic+and+Environmental+Changes+in+Global+Drylands, 2024.

Pöppl, R., Keesstra, S., and Parsons, A.: Connectivity in Geomorphology, ISBN 9781108842402, https://doi.org/10.1017/9781108903196, 2025.

Ravi, S., Breshears, D. D., Huxman, T. E., and D'Odorico, P.: Land degradation in drylands: interactions among hydrologic–aeolian erosion and vegetation dynamics, Geomorphology, 116, 236–245, 2010.

Renard, K. G.: Predicting soil erosion by water: a guide to conservation planning with the Revised Universal Soil Loss Equation (RUSLE), US Department of Agriculture, Agricultural Research Service, https://www.ars.usda.gov/research/publications/publication/?seqNo115=, 1997.

Reusser, L., Bierman, P., and Rood, D.: Quantifying human impacts on rates of erosion and sediment transport at a landscape scale, Geology, 43, 171–174, https://doi.org/10.1130/G36507.1, 2015.

Robichaud, P. R., Lewis, S. A., Wagenbrenner, J. W., Ashmun, L. E., and Brown, R. E.: Post-fire mulching for runoff and erosion mitigation: Part I: Effectiveness at reducing hillslope erosion rates, Catena, 105, 75–92, 2013.

Schindewolf, M. and Schmidt, J.: Parameterization of the EROSION 2D/3D soil erosion model using a small-scale rainfall simulator and upstream runoff simulation, Catena, 91, 47–55, 2012.

Schmidt, J.: A mathematical model to simulate rainfall erosion., Catena Supplement, https://www.sciencedirect.com/search?qs=A%20mathematical%20model%20to%20simulate%20rainfall%20erosion, 1991.

https://doi.org/10.5194/egusphere-2026-6135
Preprint. Discussion started: 22 November 2026
© Author(s) 2026. CC BY 4.0 License.



Scoging, H., Parsons, A. J., and Abrahams, A. D.: Application of a dynamic overland-flow hydraulic model to a semi-arid hillslope, Walnut Gulch, Arizona, Overland Flow: Hydraulics and Erosion Mechanics, pp. 105–145, https://search.worldcat.org/search?q=Overland+Flow+Hydraulics+and+Erosion+Mechanics+1992, 1992.

Shao, Y.: Physics and modelling of wind erosion, Springer, https://link.springer.com/book/10.1007/978-1-4020-8895-7, 2008.

Skidmore, E.: Wind erosion, in: Soil erosion research methods, pp. 265–294, Routledge, https://www.routledge.com/search?kw=Soil%20erosion%20research%20methods, 2017.

Spearman, C.: The proof and measurement of association between two things., American Journal of Psychology, https://www.jstor.org/stable/1412159, 1961.

Sporns, O., Tononi, G., and Kötter, R.: The human connectome: a structural description of the human brain, PLoS Computational Biology, 1, e42, https://doi.org/10.1371/journal.pcbi.0010042, 2005.

Strahler, A. N.: Systems theory in physical geography, Physical Geography, 1, 1–27, https://www.tandfonline.com/action/doSearch?AllField=Systems+theory+in+physical+geography, 1980.

Tatard, L., Planchon, O., Wainwright, J., Nord, G., Favis-Mortlock, D., Silvera, N., Ribolzi, O., Esteves, M., and Huang, C. H.: Measurement and modelling of high-resolution flow-velocity data under simulated rainfall on a low-slope sandy soil, Journal of Hydrology, 348, 1–12, https://doi.org/10.1016/j.jhydrol.2007.07.016, 2008.

Tiwari, S., Turnbull, L., and Wainwright, J.: Local-and global-scale hydrological and sediment connectivity over grassland and shrubland hillslopes, Journal of Hydrology, 655, 132 896, https://doi.org/10.1016/j.jhydrol.2025.132896, 2025.

Turnbull, L. and Wainwright, J.: From structure to function: Understanding shrub encroachment in drylands using hydrological and sediment connectivity, Ecological Indicators, 98, 608–618, https://doi.org/10.1016/j.ecolind.2018.11.039, 2019.

Turnbull, L., Wainwright, J., and Brazier, R. E.: Hydrology, erosion and nutrient transfers over a transition from semi-arid grassland to shrubland in the South-Western USA: A modelling assessment, Journal of Hydrology, 388, 258–272, 2010a, https://doi.org/10.1016/j.jhydrol.2010.05.005.

Turnbull, L., Wainwright, J., Brazier, R. E., and Bol, R.: Biotic and abiotic changes in ecosystem structure over a shrub-encroachment gradient in the Southwestern USA, Ecosystems, 13, 1239–1255, 2010b, https://doi.org/10.1007/s10021-010-9384-8.

Turnbull, L., Wilcox, B. P., Belnap, J., Ravi, S., D'odorico, P., Childers, D., Gwenzi, W., Okin, G., Wainwright, J., Caylor, K., et al.: Understanding the role of ecohydrological feedbacks in ecosystem state change in drylands, Ecohydrology, 5, 174–183, https://doi.org/10.1002/eco.265, 2012.

Turnbull, L., Hütt, M.-T., Ioannides, A. A., Kininmonth, S., Poeppl, R., Tockner, K., Bracken, L. J., Keesstra, S., Liu, L., Masselink, R., et al.: Connectivity and complex systems: learning from a multi-disciplinary perspective, Applied Network Science, 3, 1–49, https://doi.org/10.1007/s41109-018-0067-2, 2018.

Voutsa, V., Battaglia, D., Bracken, L. J., Brovelli, A., Costescu, J., Diaz Munoz, M., Fath, B. D., Funk, A., Guirro, M., Hein, T., et al.: Two classes of functional connectivity in dynamical processes in networks, Journal of the Royal Society Interface, 18, 20210 486, https://doi.org/10.1098/rsif.2021.0486, 2021.

Wainwright, J., Parsons, A. J., and Abrahams, A. D.: A simulation study of the role of raindrop erosion in the formation of desert pavements, Earth surface processes and landforms, 20, 277–291, 1995., https://dur.ac.uk/staff/john-wainwright/.

Wainwright, J., Parsons, A. J., and Abrahams, A. D.: Field and computer simulation experiments on the formation of desert pavement, Earth Surface Processes and Landforms, 24, 1025–1037, 1999., https://dur.ac.uk/staff/john-wainwright/.

https://doi.org/10.5194/egusphere-2026-6135
Preprint. Discussion started: 22 November 2026
© Author(s) 2026. CC BY 4.0 License.



Wainwright, J., Parsons, A. J., Müller, E. N., Brazier, R. E., Powell, D. M., and Fenti, B.: A transport-distance approach to scaling erosion rates: 1. Background and model development, Earth Surface Processes and Landforms, 33, 813–826, 2008a, https://doi.org/10.1002/esp.1624.

Wainwright, J., Parsons, A. J., Müller, E. N., Brazier, R. E., Powell, D. M., and Fenti, B.: A transport-distance approach to scaling erosion rates: 2. Sensitivity and evaluation of MAHLERAN, Earth Surface Processes and Landforms, 33, 962–984, 2008b, https://dur.ac.uk/staff/john-wainwright/.

Wainwright, J., Parsons, A. J., Müller, E. N., Brazier, R. E., Powell, D. M., and Fenti, B.: A transport-distance approach to scaling erosion rates: 3. Evaluating scaling characteristics of Mahleran, Earth Surface Processes and Landforms, 33, 1113–1128, 2008c, https://dur.ac.uk/staff/john-wainwright/.

Wischmeier, W. H. and Smith, D. D.: Predicting rainfall erosion losses: a guide to conservation planning, 537, Department of Agriculture, Science and Education Administration, https://naldc.nal.usda.gov/catalog/CAT79706928, 1978.

Yadav, A. C., Quadir, A., and Jafri, H. H.: Finite-size scaling of critical avalanches, Physical Review E, 106, 014 148, https://doi.org/10.1103/PhysRevE.106.014148, 2022.

https://doi.org/10.5194/egusphere-2026-6135
Preprint. Discussion started: 22 November 2026
© Author(s) 2026. CC BY 4.0 License.

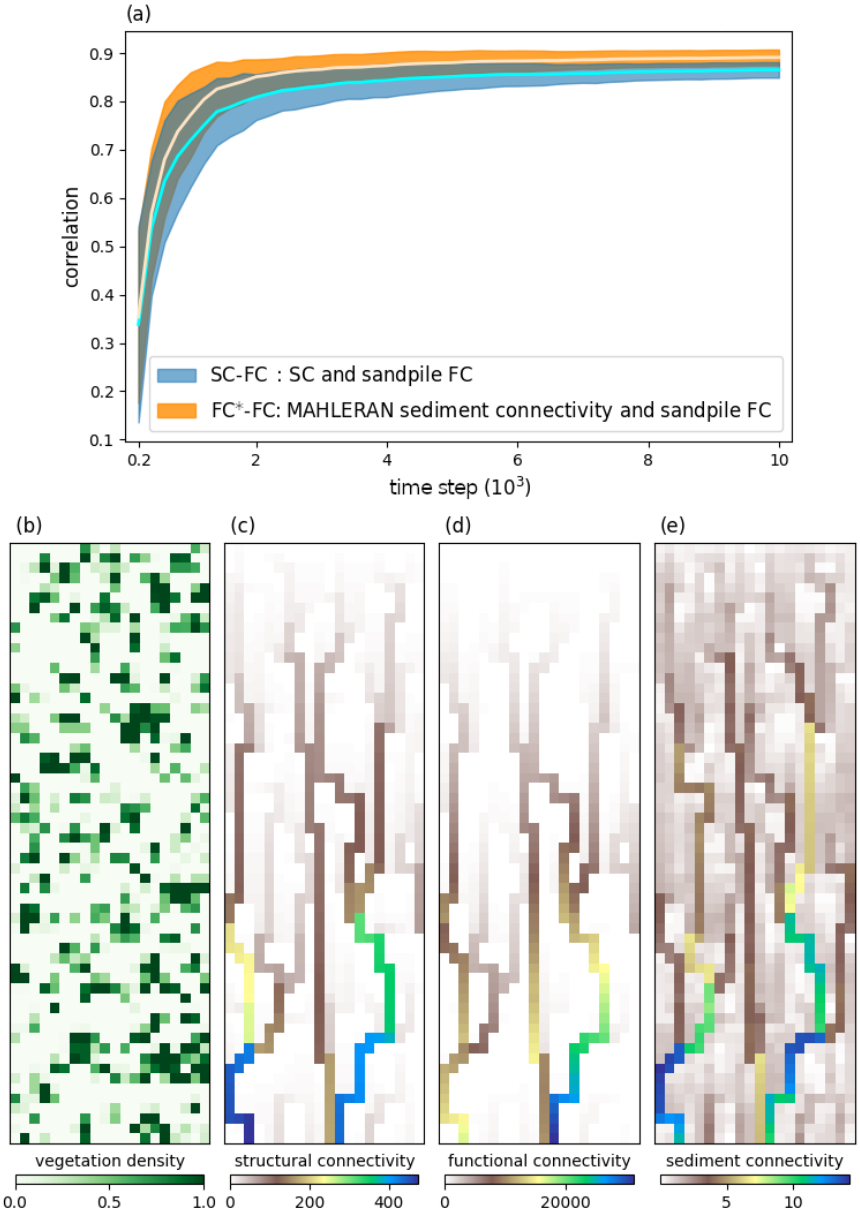


Figure 3. Deterministic descent sandpile dynamics converge towards MAHLERAN simulation outputs on shrubland. (a) Time evolution of the Pearson correlation coefficient between the sandpile functional connectivity FC (see Section 2.6.2) and the structural connectivity SC (blue band), and the MAHLERAN sediment connectivity FC* (orange band) on shrubland. Correlations are averaged from 100 simulations considering *deterministic* descent dynamics for 10^4 time steps and are shown as bands (standard deviation) within which the mean is indicated by a line. **(b)** Vegetation density on shrubland. **(c)** Structural connectivity SC measured on shrubland. **(d)** Sandpile functional connectivity FC measured at the end of one of the 100 simulations used in (a). **(e)** MAHLERAN sediment connectivity FC* measured on shrubland. The Pearson correlation coefficient between (c) and (d) is equal to 0.87, and between (c) and (e) is equal to 0.91.

https://doi.org/10.5194/egusphere-2026-6135
Preprint. Discussion started: 22 November 2026
© Author(s) 2026. CC BY 4.0 License.

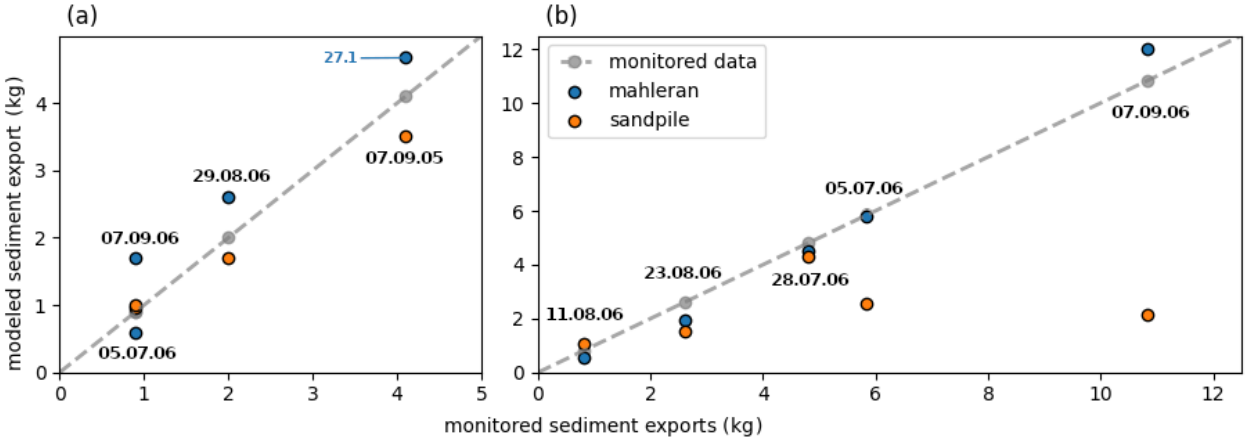


Figure 4. Comparison of sediment exports on (a) grassland and (b) shrubland between monitored empirical data (one-to-one diagonal grey dashed line), simulation data modeling with MAHLERAN (blue dots) and the sandpile model with deterministic descent dynamics (orange dots). Each date along the x-axis indicates the day in which the empirical data was monitored. The empirical data is comprised of both rainfall time-series (used as input to MAHLERAN and the sandpile model) and corresponding sediment exports measured at the hillslope plot outlet.

https://doi.org/10.5194/egusphere-2026-6135
Preprint. Discussion started: 22 November 2026
© Author(s) 2026. CC BY 4.0 License.

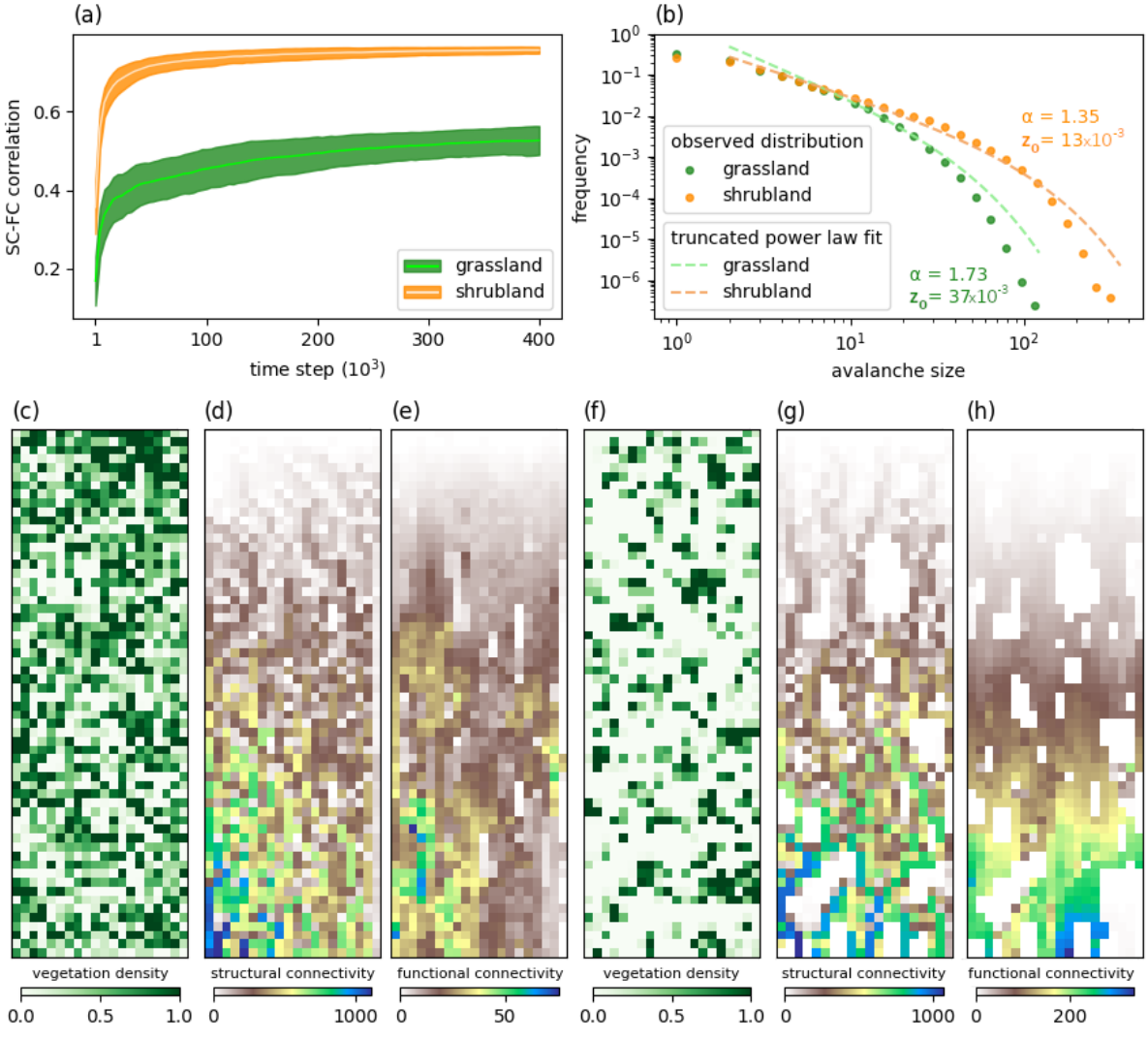


Figure 5. Probabilistic descent sandpile dynamics on grassland and shrubland. **(a)** Time evolution of SC-FC correlations $\rho^{\mathbb{G}}$ on grassland (green band) and $\rho^{\mathbb{S}}$ on shrubland (orange band). Each ρ is averaged from 100 simulations considering probabilistic descent dynamics for 4×10^5 time steps and are shown as bands (standard deviation) within which the mean is indicated by a line. **(b)** Avalanche size distributions accumulated on grassland (green dots) and shrubland (orange dots) during the simulations used in (a), and fitted with an exponentially truncated power law (green and orange dashed curves, respectively). α and z_0 denote their respective scaling exponents and cut-off parameters. **(c)** Vegetation density on grassland. **(d)** SC measured on grassland. **(e)** FC measured on grassland in one of the 100 simulations on used in (a). **(f)** Vegetation density on shrubland. **(g)** SC measured on shrubland. **(h)** FC measured on shrubland in one of the 100 simulations on used in (a). For the representative FC realisations shown in (e) and (h), $\rho^{\mathbb{G}} = 0.61$ and $\rho^{\mathbb{S}} = 0.78$, respectively.

https://doi.org/10.5194/egusphere-2026-6135
Preprint. Discussion started: 22 November 2026
© Author(s) 2026. CC BY 4.0 License.

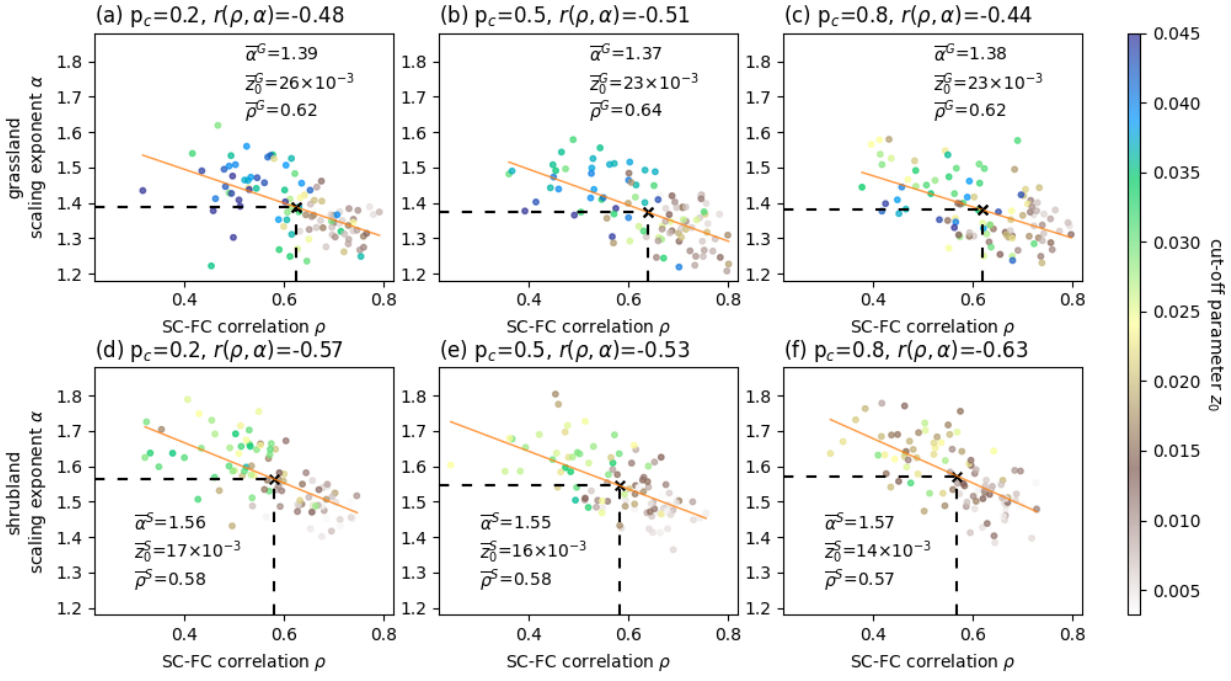


Figure 6. Heavy-tailedness of avalanche size distributions and SC-FC correlations on generated shrublands versus grasslands. Heavy-tailedness measured by the scaling exponent α and the cut-off parameter z_0 of a fitted exponentially truncated power law. The first and second rows represent the results obtained on generated grasslands and shrublands, respectively, for varying vegetation clustering probability $p_c = 0.2, 0.5, 0.8$ along the columns, from left to right. **(a)**, **(b)** and **(c)** illustrate the cut-off parameters z_0 (y-axis) as a function of ρ (x-axis) and the scaling exponent α (color) on 100 generated grasslands for each clustering probability. **(d)**, **(e)** and **(f)** illustrate the same relationship, but on shrublands. The observed Pearson correlation r between ρ (x-axis) and α (y-axis) is indicated above each corresponding scatter plot. Each data point represents the average value observed at the end of 100 simulations considering probabilistic descent dynamics for 10^5 steps. Each dashed vertical and horizontal line represent $\overline{\rho}$ and $\overline{\alpha}$ respectively, the average ρ and α observed for the given sample landscape and p_c, respectively.